A holistic model-less approach for the optimal real-time control of power electronics-dominated AC microgrids

J. Carlos Olives-Camps, Álvaro Rodríguez del Nozal, Juan Manuel Mauricio, José María Maza-Ortega *

Department of Electrical Engineering, Universidad de Sevilla, Camino de los descubrimientos s/n, Seville, 41092, Spain

ARTICLE INFO

ABSTRACT

This paper addresses the problem of optimally operating a set of grid-forming devices in an AC microgrid when a detailed network model is not available. The main aim of the approach is to maximize the power sharing of the controllable grid-forming devices and to maintain the frequency and the nodal voltages of the microgrid as close as possible to their corresponding references. The proposed control architecture is conformed by a local control layer in each grid-forming device that intends to emulate the performance of a synchronous machine and a centralized secondary controller composed of two complementary tools that coordinates the setpoints of the grid-forming devices: an online feedback optimization algorithm and an automatic generation control. The proposed method has been validated through simulations and hardware-in-the-loop tests, evidencing its good performance and robustness under different conditions.

1. Introduction

Accelerating the decarbonization of the generation mix and improving the energy efficiency are the cornerstones of the global response to mitigate the effects of the climate crisis and guarantee energy access throughout the world. For this reason, the massive integration of renewable energy sources (RES) into power systems is the roadmap of the United States, China, India and the European Union, which recently reinforced their commitment to accelerate their deployment [1]. The vast majority of RESs are directly connected to the bulk power system through power electronic converters. Therefore, in the near future, power systems are expected to be dominated by these converter-interfaced generators (CIGs) instead of the traditional synchronous technology.

In addition, this technological change unlocks the use of small-scale CIGs connected to distribution levels. Bringing the generation close to the load offers numerous advantages compared to the traditional solution based on large power plants connected to the transmission system. As a result, alternative network operation approaches emerge, being *microgrids* one of the most prominent concepts in the last decades [2,3]. A microgrid (MG) is a small low-voltage grid that includes loads and generation that can be operated locally as a single controllable entity. MGs typically have the ability to operate connected to the bulk power system through a point-of-common coupling (PCC) or as an islanded system. These different operation modes have a determinant impact on

the CIG controller type. In case of grid-connected operation, CIGs can be operated as grid-feeding devices [4], since the voltage characteristics (amplitude and frequency) are imposed by the external grid. On the contrary, the islanded operation requires the use of some CIGs with grid-forming capability to set the voltage [5]. However, considering the gradual decommissioning of conventional synchronous assets, grid-forming CIGs will be required along the power system to contribute to the network support, since the traditional assumption of strong voltage will no longer be valid [6]. For this reason, several control strategies dealing with the implementation of the grid-forming capability have appeared in recent years: droop [7], virtual impedance [8], virtual synchronous machine [9], virtual oscillator control [10] and synchronous power control [11], among others. Most grid-forming controllers provide similar steady-state performance in terms of local voltage regulation, frequency control contribution and load balancing, but subtle differences appear under transient conditions [12].

On the other hand, MGs, as single controllable entities, are equipped with controllers responsible for coordinating the operation of the different controllable assets [13]. In this regard, different approaches have been proposed: centralized [14–16] or distributed [17–19]. In any case, this MG controller can be considered as a secondary control layer responsible for computing the setpoints for the controllable assets. Traditionally, optimization theory has been applied in secondary control layers to obtain an optimal operation considering all the constraints of

---

* Corresponding author.
  E-mail address: jmmaza@us.es (J.M. Maza-Ortega).

the power system [20]. To do so, the optimization problem is solved by considering load/generation forecasts and a steady-state non-linear system model [21]. To reduce the computational cost, model simplification [22], convex relaxation [23] and approximation techniques [24] have been successfully applied. Once computed, the optimal setpoints are updated and broadcasted to the controllable units that apply them to the power system in a feedforward manner. However, considering that the setpoints are usually updated in a time frame of minutes, these strategies may become inadequate for future power systems due to volatile conditions of both generation and consumption [25]. An alternative to this methodology is the online feedback optimization (OFO) paradigm, which establishes a feedback interconnection between the optimization algorithm and the physical system. In the OFO approach, a real-time optimization algorithm computes a control action considering the field measurements and applies it to the system. The computation of this control action does not require precise information about the network model but just some sensitivities [26,27]. Then, the system naturally *computes* the state or output vector due to the enforcement of the physical laws. As a result, the optimization problem is solved in closed loop with the physical system [28]. Regarding the operation of the power system, OFO can be understood as a method to drive the power system to an operating point that solves an AC optimal power flow problem without resorting to the power flow equations [29].

High robustness, reduced computational effort and protection of private information make OFO a strong candidate for MG secondary control, taking advantage of the fast dynamics of power electronics devices. For these reasons, several recent works have proposed OFO-based secondary control strategies for MG. For example, OFO has been successfully applied to solve the voltage regulation of AC distribution networks by reactive power injection in [30]. Another example is [31], where a dynamic state estimation stage feeds the feedback optimization scheme to drive the controllable power injections towards the optimal setpoints. Distributed OFO implementations can also be found in the literature to solve the problem of voltage regulation in distribution networks [32,33]. Nevertheless, to the best of the authors' knowledge, all the published works have been raised considering that the controllable units operate in grid-feeding mode. This work proposes the development of a MG secondary control layer based on two complementary algorithms to coordinate several grid-forming CIGs. A conventional Automatic Generation Controller (AGC) is responsible for maintaining the frequency at its nominal value by assigning adequate active power increments to the CIGs. In addition, a non-convex OFO-based controller [34] is in charge of computing the internal voltage references of the CIGs to maintain the network voltages within the regulatory limits. Therefore, the main contributions of this work can be summarized as follows:

- Development of a hierarchical control architecture capable of managing AC MGs operating in islanding mode with 100% of RES-based CIGs.
- Development of a secondary control approach for AC MGs involving grid-forming CIGs based on two complementary algorithms for frequency and voltage regulation.
- Definition of a secondary voltage control strategy based on the model-free OFO algorithm to achieve an optimal dispatch of the grid-forming CIGs considering their operational limits.
- Regulation of the internal voltage of each controllable grid-forming CIG to achieve a high degree of active and reactive power sharing regardless of the MG R/X ratio.

The remainder of this paper is divided into the following parts. Section 2 discusses the problem of interest and establishes the objectives pursued in this work. Section 3 presents the proposed methodology: first, the implementation of a grid-forming CIG is discussed and then the secondary control strategy is detailed. Section 4 analyzes the performance of the proposed algorithm by simulations within two different MGs and a Hardware-in-the-Loop (HIL) test. This is followed by Section 5, which presents the conclusions of this work and outlines future research lines.

2. Problem description

Consider an AC MG modeled as an undirected graph $\mathcal{G} = (\mathcal{V}, \mathcal{E})$ in which $\mathcal{V}$ represents the set of buses and $\mathcal{E} \subseteq \mathcal{V} \times \mathcal{V}$ the set of power lines that interconnect those buses. Some buses, $\mathcal{V}_g \subseteq \mathcal{V}$, are powered by CIGs operating in grid-forming mode. Therefore, CIGs are able to control the voltage amplitude and frequency of their corresponding point of interconnection (POI). Furthermore, some uncontrollable loads and generators can be connected to the rest of the MG buses, $\mathcal{V} \backslash \mathcal{V}_g$.

On the basis of this framework, it is proposed that the setpoints of the grid-forming CIGs be computed by a centralized secondary control layer that includes the corresponding communication infrastructure. Moreover, it is assumed that a detailed network model is unknown. Therefore, the computation of the setpoints may rely only on the available network measurements.

The aim of the secondary control layer is to achieve a coordinated control of the MG CIGs considering the following technical objectives:

(i) Support the MG frequency regulation, minimizing the deviations with respect to the reference value.
(ii) Determine the active power injection of each CIG as a function of the frequency deviation and a participation factor, which can be adjusted considering either the CIG rated power or an economic criterion.
(iii) Maintain nodal voltages close to given reference values and within the voltage limits for every $k \in \mathcal{V}_g$.
(iv) Share the active and reactive power load demanded in the MG among the installed CIGs to prevent overloads.

3. Proposed method

This section provides all the details of the methodology applied to solve the problem posed in the previous section. For this purpose, the control architecture is presented first and follows a comprehensive description of the grid-forming CIG primary controllers. Finally, the secondary controller in charge of coordinating the control actions of the CIGs to achieve the optimal operation of the MG is outlined.

3.1. Control architecture

The proposed hierarchical two-layer control architecture designed to achieve the objectives described in the previous section is shown in Fig. 1.

The primary control layer is locally implemented in each CIG and, consequently, is able to perform fast response actions to ensure a secure MG operation. In this regard, this work proposes to emulate the performance of the synchronous generator including all its local controllers. In this manner, the CIGs may support the MG frequency with active power sharing. Since the CIG is emulating a synchronous generator, the controller setpoints are the active power and the internal voltage. All the electrical magnitudes involved in this control layer are represented in lowercase and are assumed to be updated quasi-instantaneously due to the fast actuation of the power electronics.

The secondary control layer coordinates the grid-forming CIGs with two independent complementary algorithms for the computation of the active power and the internal voltage references. The separation of these two tasks can be justified considering the different nature of the frequency and voltage control within a MG. Note that the MG frequency control can be tackled considering a single electrical node, while the MG voltage control is a local problem that depends on the power injections at each MG node. First, a conventional AGC establishes the active power setpoints for each CIG to restore the frequency to its reference, thus complementing the local $P - f$ droop control. Second, an OFO algorithm is implemented to coordinate the CIGs with the aim of improving the reactive power sharing and maintaining the nodal
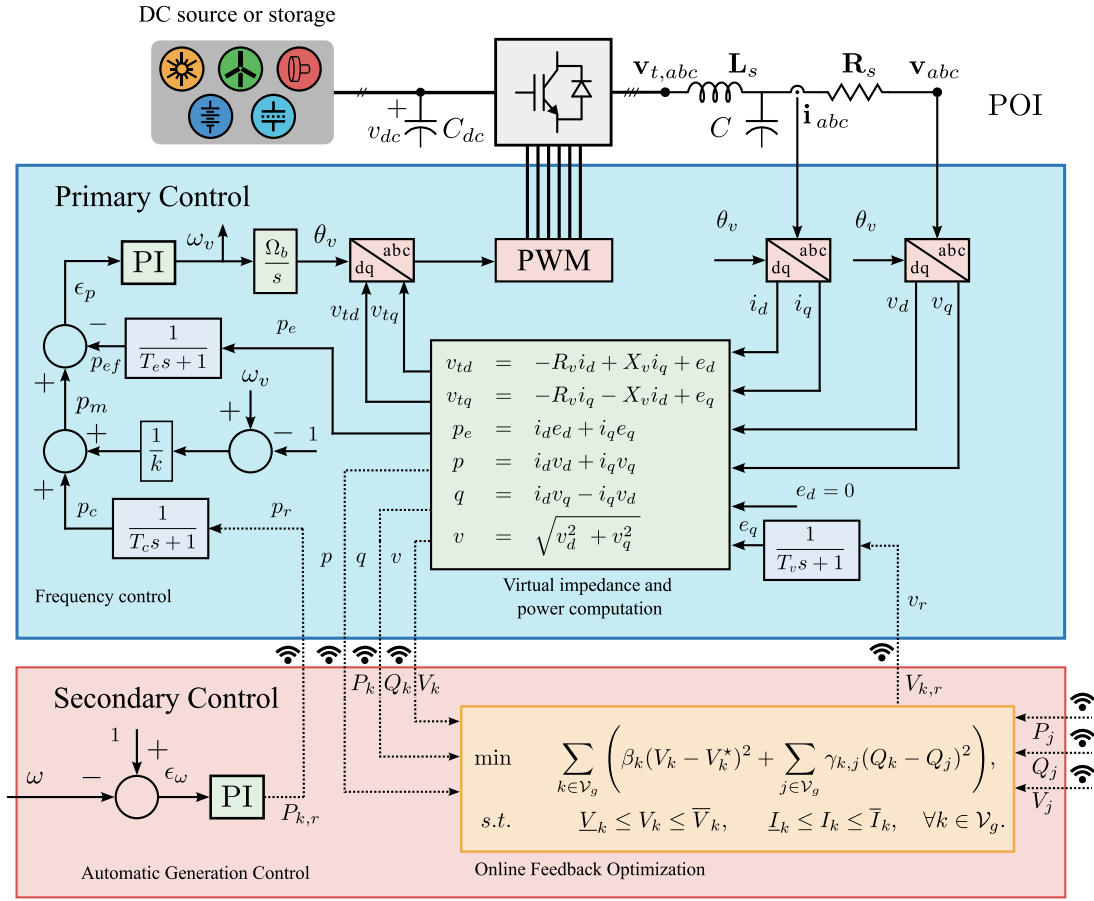
Fig. 1. Proposed hierarchical control architecture.

voltages close to the given references. The electrical magnitudes taking part in this secondary control layer are presented in capital letters and are updated after each communication cycle between the CIGs and the secondary central controller.

A more detailed description of each of these control layers follows in the next subsections.

3.2. Primary virtual synchronous generator control

The emulation of the synchronous machine implemented in this paper is based on the Proportional–Integral Virtual Synchronous Generator (PI-VSG) [35]. As in the case of a synchronous machine, the proposed PI-VSG has two main setpoints [35]: virtual electromotive force (EMF), e_q, and virtual mechanical power, p_m.

The virtual EMF, represented here by e_q, is obtained after applying a low-pass filter to the centralized secondary controller signal, v_r, which mimics the voltage setpoint of the automatic voltage regulators (AVRs) of a conventional synchronous generator.

The virtual mechanical power is calculated as the primary frequency response based on a droop control and modified with a term computed by the centralized secondary controller:

$$p_m = p_c + \frac{1}{k}\left(\omega_v - \omega^\star\right) \tag{1}$$

where p_c is the low-pass filter output of the secondary control power, p_r, k^{-1} is the frequency droop gain, ω_v and $\omega^\star$ are the virtual generator speed and its corresponding reference. This virtual mechanical power is compared with the generated electrical power to determine the power imbalance:

$$\epsilon_p = p_m - p_{ef}. \tag{2}$$

where p_{ef} is obtained by applying a low-pass filter to the instantaneous CIG output power. This power imbalance, ϵ_p, is canceled using a PI controller which is in charge of computing the virtual speed, ω_v. Finally, the integral of the virtual speed corresponds to the angle, θ_v, used in the different VSG Park transformations.

Finally, the internal voltage, v_t, is computed considering the virtual EMF, e_q, the angle, θ_v, and applying the corresponding voltage drop on a virtual impedance. This guarantees a proper active power sharing even in the case of highly resistive networks.

3.3. Secondary control

The secondary control layer is implemented in a centralized manner to collect local CIG measurements and the MG frequency. Taking into account this information, the secondary control layer computes the setpoints that are dispatched to the local primary controllers of the grid-forming CIGs: AGC active power reference, $P_{k,r}$, and voltage reference, $V_{k,r}$. These setpoints are calculated in two complementary control algorithms specifically suited for frequency and voltage control.

3.3.1. Secondary frequency control

The aim of the secondary frequency regulation is to restore the system frequency when an event occurs. A conventional AGC supports the primary droop control already implemented in the grid-forming CIGs to achieve a null frequency deviation in steady state. Typically, this is done by applying a single-node equivalent network model in which the frequency deviation is counteracted by varying the active power of the generators. In particular, the power provided by the AGC is the result of the application of a discrete-time proportional–integral (PI) control to the difference between the MG frequency and
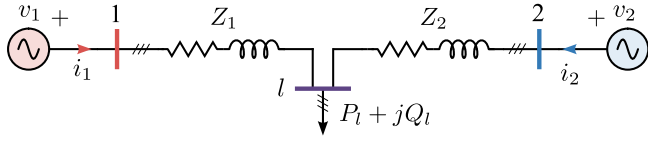
Fig. 2. One-line diagram of the simple test case.

Table 1
Parameters of the simple test case.

Parameter	Value
Rated voltage	400 V
Line impedance Z_1	$0.0287 + j0.0167\ \Omega$
Line impedance Z_2	$0.1148 + j0.0668\ \Omega$

Fig. 3. Simple test case. Simulation results comparing the proposed controller with an OPF (dotted lines). $\alpha = 8 \cdot 10^{-5}$, $\beta_k = 10^3$, $\gamma_{k,j} = 200$, $\forall k, j \in \mathcal{V}_g$. Unconstrained (blurred lines) and constrained (solid lines) optimization problems. Top plot: Frequency of the system. Bottom plot: CIG nodal voltages.

its reference:

$$P_{k,r}(m) = K_p(\omega(m) - \omega^\star) + \xi(m),$$

$$\xi(m+1) = \xi(m) + \Delta t \frac{K_p}{T_i}(\omega(m) - \omega^\star),$$

where K_p, T_i are the proportional gain and integration time of the PI controller, respectively, Δt is the communication period of the secondary control layer and m is the discrete-time step.

3.3.2. Optimal voltage regulation

This part of the secondary control layer optimally computes the voltage references, $V_{k,r}$, for each grid-forming CIG. In particular, it is proposed to minimize voltage deviations with respect to a given setpoint while maintaining a proper reactive power sharing between the CIGs. Note that the active and reactive power sharing strategy prevents the CIG overloading. As a result, the voltage references, $V_{k,r}$, can be set by solving the following optimization problem:

$$\min_{V_{k,r} \forall k \in \mathcal{V}_g} \sum_{k \in \mathcal{V}_g} \left(\beta_k (V_k - V_k^\star)^2 + \sum_{j \in \mathcal{V}_g} \gamma_{k,j}(Q_k - Q_j)^2 \right), \quad (3)$$

$$s.t. \quad \underline{V}_k \le V_k \le \overline{V}_k, \quad \underline{I}_k \le I_k \le \overline{I}_k, \quad \forall k \in \mathcal{V}_g,$$

where Q_k is the reactive power injection, V_k is the controlled nodal voltage and $V_k^\star$ is the voltage setpoint for the k-th CIG. Note that $\underline{V}_k$, $\overline{V}_k$, $\underline{I}_k$ and $\overline{I}_k$ are the voltage and current limits related to the k-th CIG which have been included in the optimization problem as inequality constraints. Furthermore, it is important to emphasize that the objective function includes two weighting parameters, namely β_k and $\gamma_{k,j}$, which must be adjusted to achieve a compromise solution between the two pursued objectives.

Note that the relationship between the input signals, $V_{k,r}$, and the output variables (nodal voltages, V_k, active and reactive power injections, P_k and Q_k), is not explicitly stated in (3). In fact, this relationship is determined by the network model, which is considered unknown in this formulation. This dependency can be mathematically expressed as follows:

$$\mathbf{y} = \mathbf{h}(\mathbf{u}, \mathbf{w}) \quad (4)$$

where $\mathbf{u} = [V_{k_1,r}, V_{k_2,r}, \ldots]^\top$ and $\mathbf{y} = [V_{k_1}, P_{k_1}, Q_{k_1}, V_{k_2}, P_{k_2}, Q_{k_2}, \ldots]^\top$ are the input and output column vectors that stack the voltage control variables and the nodal voltages, active and reactive power injections of all the grid-forming CIGs, respectively; $\mathbf{w}$ is a vector that stacks the unmeasured power injections/demands of the rest of the MG buses, $\mathcal{V} \setminus \mathcal{V}_g$.

The optimization problem (3) can be solved by applying the OFO control scheme presented in [34]. At each iteration, this method updates the optimal reference points, $V_{k,r}$, from the real-time measurements communicated by the CIGs. Then, these setpoints are applied to the physical system, i.e. controllable grid-forming CIGs. This two-step process is repeated iteratively until the system reaches an optimal
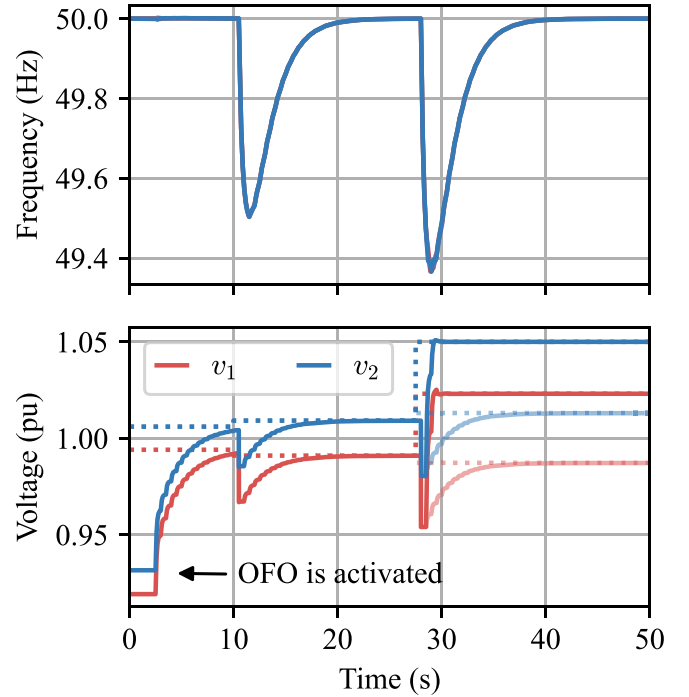
solution. Note that the computation of the control variables is based on the evolution of real-time measurements rather than on estimates based on network models.

The optimization problem (3) can be written in a compact form as:

$$\min_{\mathbf{u}} J = (\mathbf{y} - \mathbf{y}^\star)^\top \mathbf{Q}(\mathbf{y} - \mathbf{y}^\star), \quad (5)$$

$$s.t. \quad \mathbf{g}(\mathbf{y}) \le \mathbf{0},$$

where matrix $\mathbf{Q}$ encapsulates the weighting parameters β_k and $\gamma_{k,j}$, the output vector $\mathbf{y}^\star$ stacks the references of the electrical magnitudes and $\mathbf{g}(\mathbf{y}) \le \mathbf{0}$ is the set of inequality constraints.

It is well known that the gradient descent direction for the input vector in case of an unconstrained optimization problem is given by [36]:

$$\Delta \mathbf{u}^\star = -\partial J / \partial \mathbf{u} = -2\mathbf{H}^\top \mathbf{Q}(\mathbf{y} - \mathbf{y}^\star) \quad (6)$$

where $\mathbf{H}$ corresponds to the sensitivity matrix that relates inputs, $\mathbf{u}$, and outputs, $\mathbf{y}$, around an operational point:

$$\mathbf{H} = \begin{bmatrix} \frac{\partial V_{k_1}}{\partial V_{k_1,r}} & \frac{\partial V_{k_1}}{\partial V_{k_2,r}} & \cdots \\ \frac{\partial P_{k_1}}{\partial V_{k_1,r}} & \frac{\partial P_{k_1}}{\partial V_{k_2,r}} & \cdots \\ \frac{\partial Q_{k_1}}{\partial V_{k_1,r}} & \frac{\partial Q_{k_1}}{\partial V_{k_2,r}} & \cdots \\ \vdots & \vdots & \ddots \end{bmatrix}$$

However, solving problem (5) requires considering the optimization within the feasible subsets imposed by the operating constraints. Therefore, to solve (5) a projected gradient descent scheme is adopted:

$$\min_{\Delta \mathbf{u}} \|\Delta \mathbf{u} + 2\mathbf{H}^\top \mathbf{Q}(\mathbf{y}(m) - \mathbf{y}^\star)\|_2^2, \quad (7)$$

$$s.t. \quad \mathbf{g}(\mathbf{y}(m) + \alpha \mathbf{H} \Delta \mathbf{u}) \le \mathbf{0},$$

where α is the step size along the gradient descent direction. Considering this formulation, the m-th iteration of the OFO approach is outlined as follows:
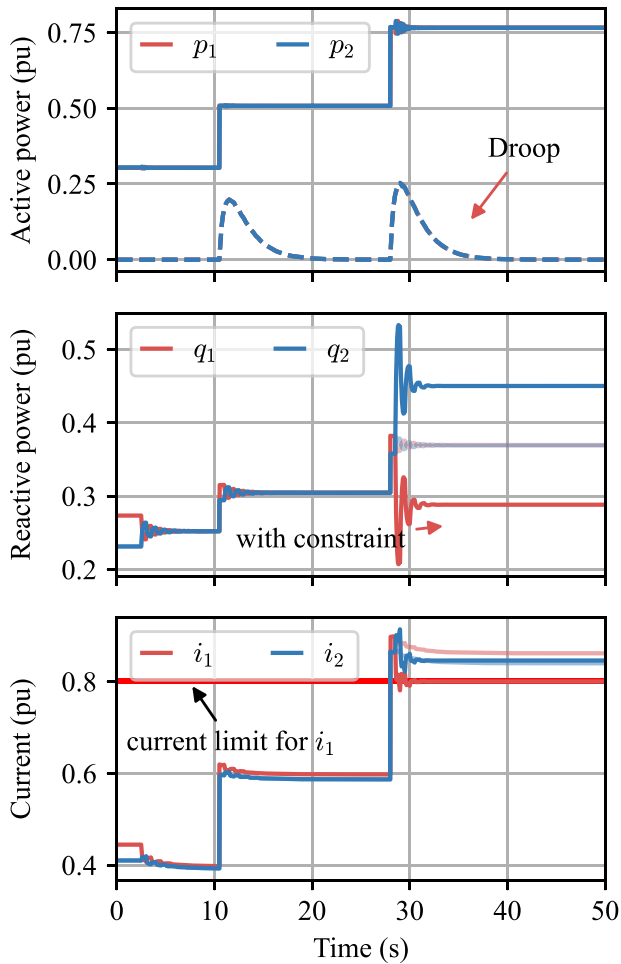
Fig. 4. Simple test case. $\alpha = 8 \cdot 10^{-5}$, $\beta_k = 10^3$, $\gamma_{k,j} = 200$, $\forall k, j \in \mathcal{V}_g$. Unconstrained (blurred lines) and constrained (solid lines) optimization problems. Top plot: Active power injection of the CIGs and contribution of the local droop. Middle plot: Reactive power injections of the CIGs. Bottom plot: Current injections of the CIGs.

1. The output signals of each grid-forming CIG are collected by the central controller that constructs the output vector $\mathbf{y}(m)$.
2. The central controller solves the constrained optimization problem posed by (7) to obtain the input vector decrement: $\Delta\mathbf{u}(m)$.
3. The input variables are updated following the gradient descent direction: $\mathbf{u}(m+1) = \mathbf{u}(m) + \alpha\Delta\mathbf{u}(m)$.
4. The new references are dispatched to each device, updating their internal signals $V_{k,r}(m+1)$.

Note that this formulation assumes that the sensitivity matrix $\mathbf{H}$ is known or measured. In fact, $\mathbf{H}$ can be computed by perturbing each input signal at once and measuring the system output [37]–[38]. Finally, and for clarification purposes, an explanatory example detailing how to formulate the problem in this compact form can be found in Appendix.

4. Performance assessment

In this section, the dynamic performance of the proposed control scheme is evaluated on two different MGs. The first one is conformed by two grid-forming CIGs feeding a load. This simple system is used to analyze the performance under constrained scenarios, the influence of the weighting parameters within (3) and possible implementation limitations through a HIL test. After that, some simulations are conducted on a MG based on the topology of the CIGRE European LV benchmark
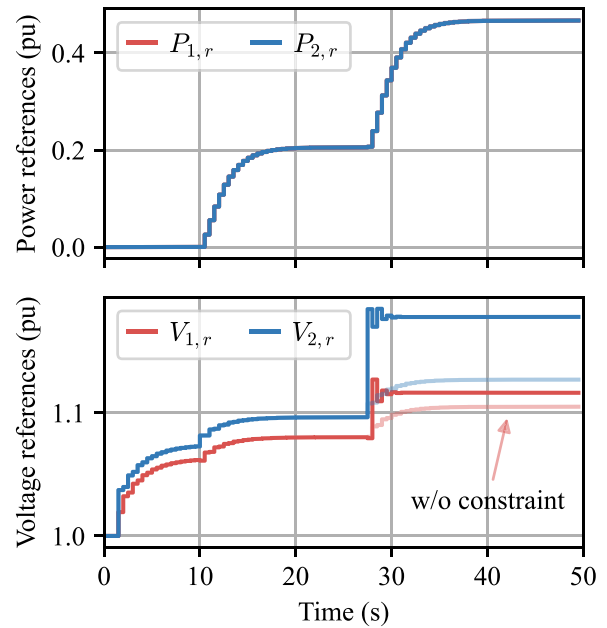

Fig. 5. Simple test case. $\alpha = 8 \cdot 10^{-5}$, $\beta_k = 10^3$, $\gamma_{k,j} = 200$, $\forall k, j \in \mathcal{V}_g$. Unconstrained (blurred lines) and constrained (solid lines) optimization problems. Top plot: Active power references of the AGC. Bottom plot: Internal voltage references of the OFO-based controller.

distribution network [39], to evidence the good performance in case of application to a larger system.

4.1. Simple test case

The simple 3-bus and 2-line LV system depicted in Fig. 2, where two grid-forming CIGs feed a load, is considered. The network parameters are listed in Table 1. Note that the difference between line impedances hampers the load power sharing between grid-forming CIGs. For simplicity and without loss of generality, grid-forming CIGs have the same rated power, 50 kVA. Furthermore, the current of the CIG at bus 1 has been constrained to 0.8 p.u. and the nodal voltages must be within [0.95 1.05] p.u. Both CIGs are initialized with $P_{k,r} = 0.0$ p.u. and $V_{k,r} = 1.0$ p.u. After two seconds of operation, the secondary control is activated with a communication period set to 0.5 s. Initially, the load is $30+j25$ kVA, but increases to $50+j30$ kVA and $75+j36$ kVA at $t = 10$ s and $t = 28$ s, respectively.

4.1.1. Comparison with the model-based OPF results

The aim of this subsection is to analyze the dynamic performance of the proposed OFO-based controller and compare it with the classical approach based on an Optimal Power Flow (OPF) algorithm where the network model is required. For this purpose, the previously described system is simulated using an electromechanical model with a simulation step of 1 ms. Fig. 3 shows the evolution of the frequency and voltage measured at buses 1 and 2. In turn, Fig. 4 illustrates the active power, reactive power and current injected by each CIG. Finally, Fig. 5 depicts the CIG references computed by the secondary controller.

The first load increase at $t = 10$ s clearly produces a frequency drop, as can be seen in Fig. 3, but the frequency is restored to its reference value due to the additional active power injections of the CIGs, detailed in Fig. 4. Note that this power increase is the result of the joint action of the local primary droop control, represented in dashed lines within Fig. 4, and the AGC implemented in the secondary control layer, as shown in Fig. 5. As expected, the AGC provides the same per unit reference to each device and recovers the frequency to its nominal value. This load increase also results in a voltage drop, as
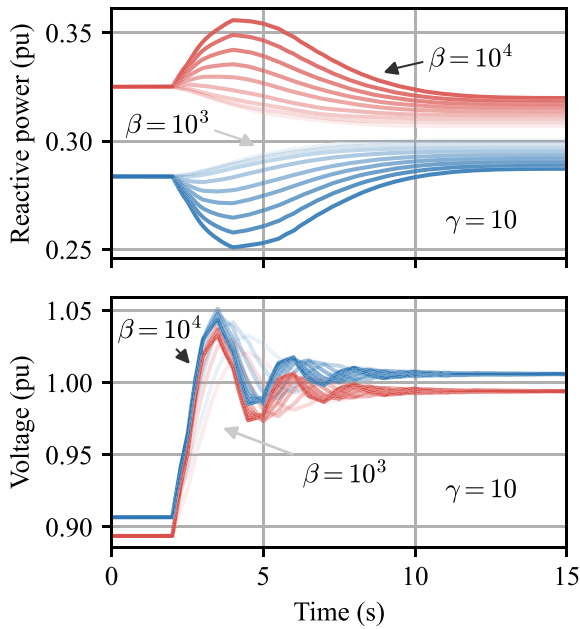
Fig. 6. Simple test case. Influence of weighting factors ($\alpha = 1.5 \cdot 10^{-4}$). OFO is activated at $t = 2$ s. Top plot: CIG reactive power. Bottom plot: CIG internal voltage.
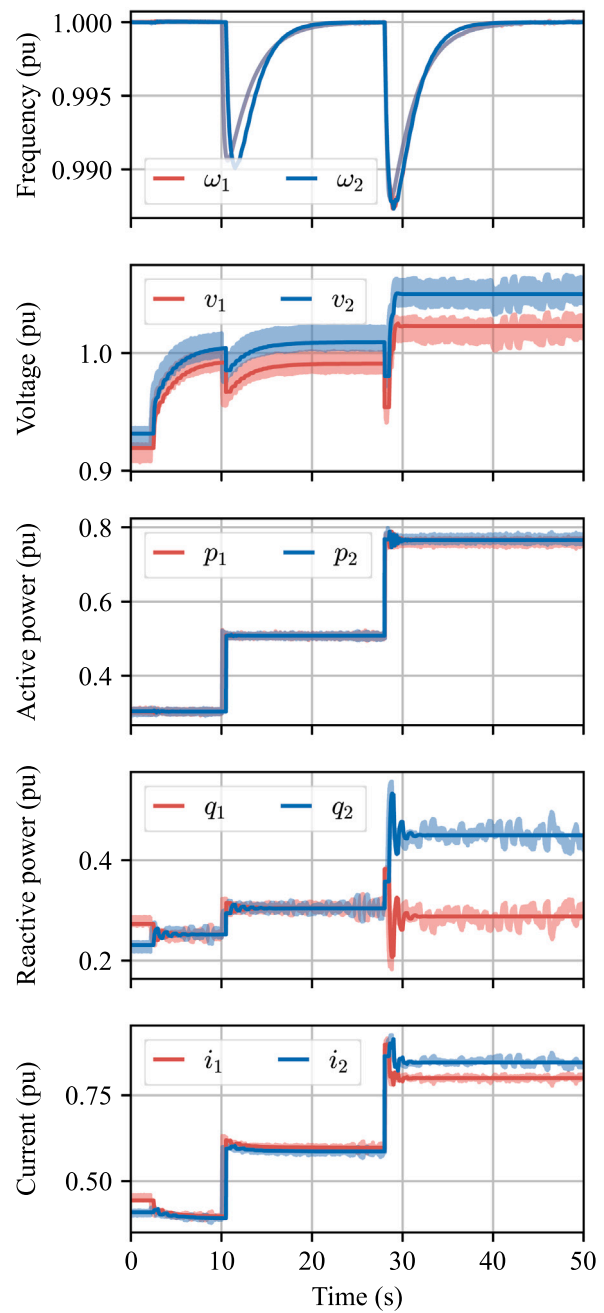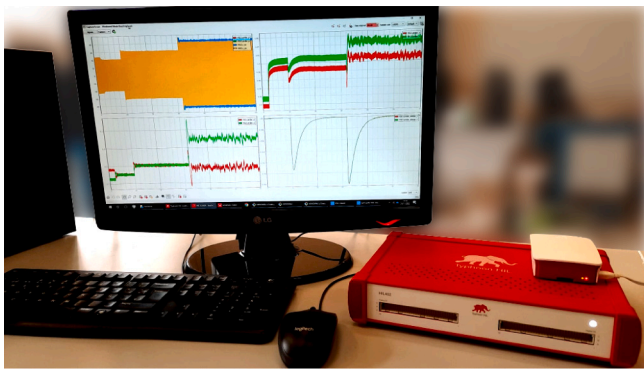

Fig. 7. Typhoon HIL-402 testing platform.

Fig. 8. Simple test case. HIL validation.

shown in Fig. 3, due to the corresponding additional injected current. As a result, the OFO-based secondary controller increases the internal voltage references of the grid-forming CIGs, as depicted in Fig. 5. In this regard, the OFO-based controller is able to maintain the voltages within the limits with an almost perfect reactive power sharing between the CIGs.

Moreover, it is important to highlight that Fig. 3 shows in dotted lines the optimal reference voltages computed by an OPF considering a detailed network model. As can be seen, the proposed OFO-based secondary controller, without the need of the network model, converges to the OPF solution in a short time period, particularly less than 10 s after its activation.

The disturbance caused by the additional load increase at t=28 s creates an interesting situation, since the current limit of the CIG connected at bus 1 is overpassed, as shown in Fig. 4. As a result, the OFO-based secondary controller modifies the internal voltage references to maintain this current within the limits. In this regard, Fig. 5 compares the internal voltage references of the constrained and unconstrained scenarios, which have been represented in solid and blurred lines, respectively. Note that it is required to reduce the contribution of

the CIG at bus 1. For this purpose, the secondary OFO-based controller increases the internal voltage reference of the CIG at bus 1 with the aim of maintaining the active power injection to the load with a lower current. In addition, note that the fulfillment of the current limit requires a drastic reduction of the reactive power injection. As a result, the OFO-based controller increases the internal voltage reference of the CIG at bus 2 which is in charge of providing most of the load reactive power. Note that the difference in the internal voltages of the CIGs is larger in this constrained situation. This clearly has an impact on the reactive power sharing which cannot be maintained, as shown in Fig. 4, to fulfill the imposed current limit. This is one of the most interesting features of the OFO methodology since the obtained steady state is within the feasible region determined by the problem constraints.
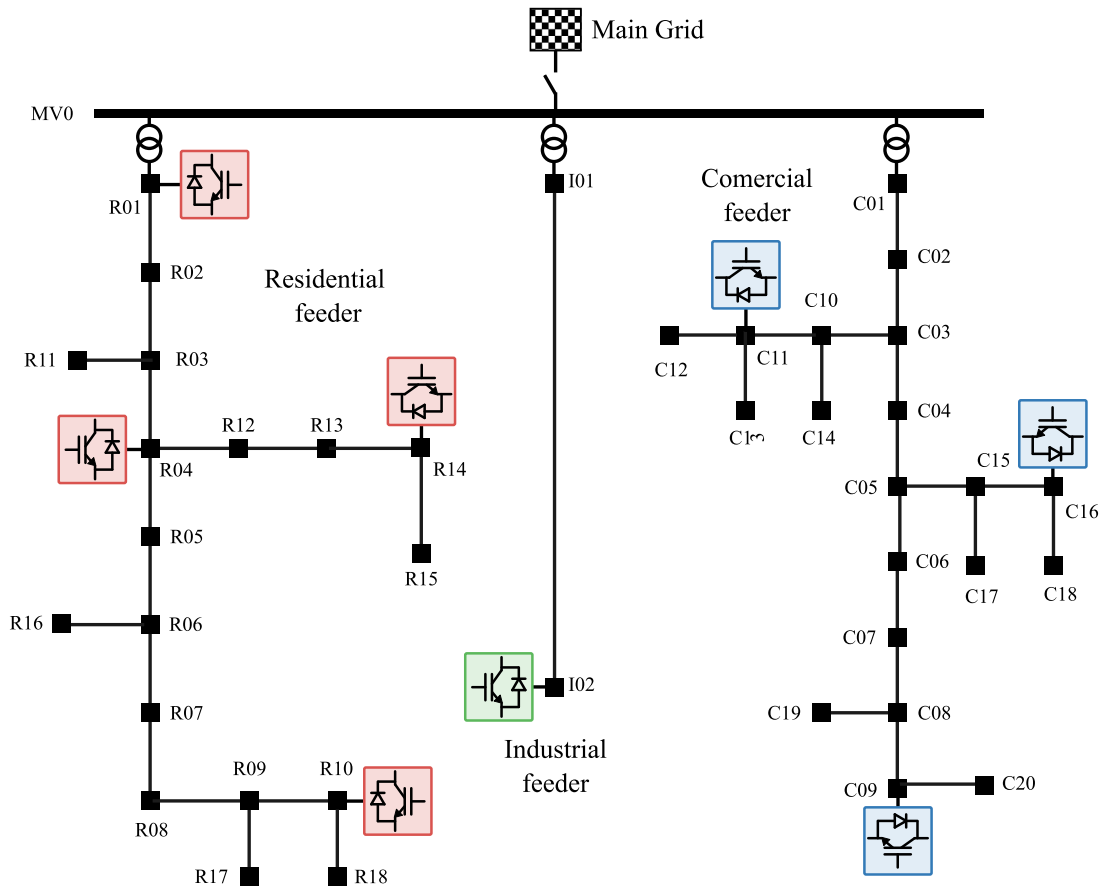
Fig. 9. MG one-line diagram based on the CIGRE European LV benchmark distribution network including the considered grid-forming CIGs.

4.1.2. Influence of the OFO-based parameters

This subsection analyzes the influence of the weighting factors used within the cost function in (3) for the optimal voltage regulation. Fig. 6 evaluates the effect of changing the ratio between β_k and $\gamma_{k,j}$ in terms of nodal voltages and reactive power injections. In particular, fixed $\gamma_{k,j} = 10$ and different values of β_k have been assumed in the interval $[10^3, 10^4]$. The simulations have been done with the initial conditions of the previously analyzed scenario but without any load variation. As expected, the lower β_k the better reactive power sharing capability between the grid-forming CIGs and, consequently, the better current sharing. Furthermore, due to the high MG R/X ratio, the improvement in the reactive power sharing capability apparently does not increase the difference between the steady-state nodal voltages and their references, which have been set to 1.0 p.u. Therefore, it is proposed to choose a lower β_k to prioritize reactive power sharing to prevent CIG overloads.

4.1.3. Hardware-in-the-loop validation

The above results have demonstrated the applicability of the proposed control architecture in the electromechanical domain. This subsection introduces the validation of the proposed controller in a HIL testing environment. For this purpose, the Typhoon HIL-402 platform shown in Fig. 7 has been used to implement the simple test case previously used in the simulation stage. All the physical components (i.e. grid-forming CIGs, load and lines) have been modeled within the FPGA subsystem with a simulation step of 1 μs. It is worth noting that a detailed CIG electromagnetic model has been used, including PWM generation and IGBT deadtime. Meanwhile, the primary control layer described in Section 3.2 has been integrated within the DSP subsystem with an execution interval of 50 μs. Finally, the proposed secondary controller has been embedded within a Raspberry Pi model

3 that is communicated through Ethernet using the UDP protocol with the Typhoon host computer. The secondary controller computes the required setpoints for the primary control layers at regular intervals of 0.5 s using the corresponding measurements. Therefore, this HIL-based validation mimics all the issues (i.e. different time scales, different hardware platforms and communication system) of an actual controller implementation.

Fig. 8 depicts the evolution of the HIL (blurred lines) and simulated (solid lines) magnitudes. As expected, the results obtained in the HIL implementation are practically the same as those obtained with the electromechanical simulation. The slight differences that can be noticed are due to the high detail model implemented in the HIL platform (LC coupling filter with passive damping, IGBT deadtime, PWM switching and realistic processing of measurements including noise and antialising filters). Therefore, this HIL testing evidences the applicability of the proposed controller in a realistic scenario and allows to validate the electromechanical simulations.

4.2. Application to a larger system

In this section, the scalability of the proposed method is tested on a MG based on the CIGRE European LV benchmark distribution network [39], which is assumed to be islanded from the MV power grid. The network is composed of three feeders (residential, industrial and commercial), as shown in the one-line diagram depicted in Fig. 9. The location of the grid-forming CIGs is also detailed in this one-line diagram. Note that the HIL validation presented in the previous section allows to rely on electromechanical simulations, which considerably reduce the execution time and the computational cost related to larger systems.
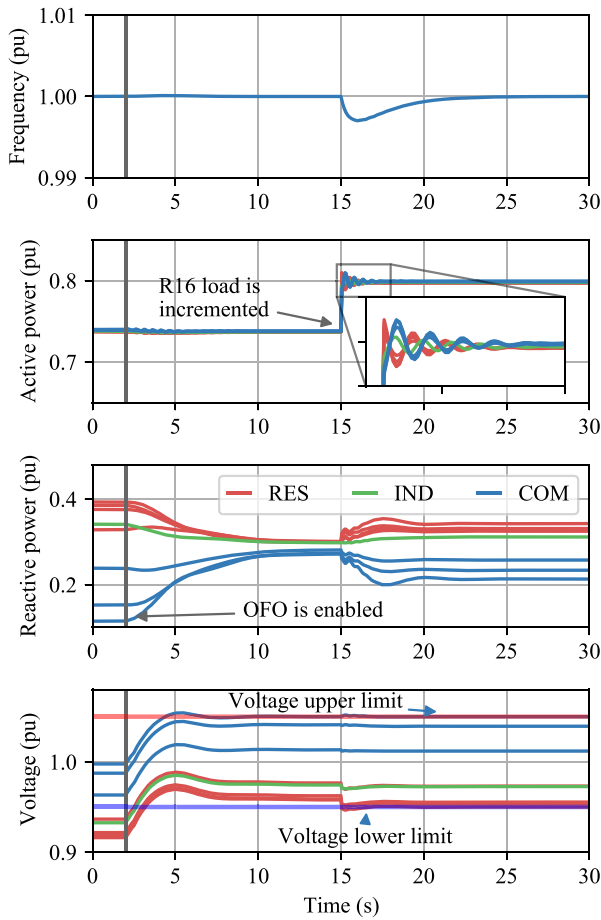
Fig. 10. MG based on the CIGRE European LV benchmark network. Short-time simulation to evidence the dynamic performance of the proposed controller. $\alpha = 0.5 \cdot 10^{-4}$, $\beta_k = 500$, $\gamma_{k,j} = 10$, $\forall k, j \in \mathcal{V}_g$.

First, the dynamic performance of the algorithm is analyzed by running a short-time simulation, which is detailed in Fig. 10. For this purpose, the same load scenario as the one proposed in [39, Section 7] has been used, with all the power demands particularized at 20:00 h. The secondary control layer is activated at $t = 2$ s, while a 44 kW load increment is produced at $t = 15$ s in bus R16 reproducing the connection of two electrical vehicle chargers.

Fig. 10 depicts the evolution of the network frequency, the nodal voltages and the CIG power injections. Three different colors have been used in the figure to differentiate the CIG locations within the residential (red), industrial (green) and commercial (blue) feeders in a similar manner than in the one-line diagram detailed in Fig. 9. As shown, before the secondary controller activation, some of the nodal voltages take values below the imposed lower limit due to the high power demand compromising the MG operation. On the contrary, all the nodal voltages are within the imposed regulation band after the secondary controller activation while sharing the required reactive power injections. Only some slight differences can be observed between the CIG reactive power injections when the steady state is reached (around $t = 14$ s) due to the necessary fulfillment of the operational constraints imposed to the nodal voltages. In this regard, note that one CIG at the commercial feeder reaches the maximum permissible voltage which leads to a decrement of its reactive power injection. When the load at bus R16 increases at $t = 15$ s, the primary control layer ensures the active power sharing within the MG CIGs. As shown, there is a frequency drop due to the demand increase that is counteracted by the inertial response given by the grid-forming CIGs, the subsequent action

of the primary frequency response and, finally, the AGC implemented in the secondary controller. As a result, the MG frequency reaches the steady-state condition in a short time period of less than 10 s. From the MG voltage point of view, the load increment results in a voltage drop in the residential feeder nodes, leading to an increase of the corresponding CIG reactive power injections. This increment seeks to raise the nodal voltages to meet the lower limit. On the other hand, CIGs within the commercial feeder decrease their reactive power injection as a result of the MG islanded operation. In fact, the increase of the reactive power injection at the residential feeder has to be compensated by a decrement within the commercial one to meet the reactive power balance. Moreover, it is interesting to note that some nodal voltages within the commercial feeder are close to the upper limit. Consequently, the reactive power injections are unevenly shared between the CIGs connected to this feeder to fulfill the technical constraints. Note that although reactive power sharing is not fully achieved, the operating constraints are always met and the OFO-based secondary controller drives the system to the optimal operating point, even in this constrained situation, evidencing its robustness.

Finally, a 24-hour simulation is conducted to assess the impact that the proposed OFO-based control algorithm may have in a large time scale. In this regard, the proposed daily load curves in [39, Section 7] has been used with updates every 10 min.

Fig. 11 compares the performance of the secondary controller with (blue color) and without (red color) the OFO-based algorithm for voltage control and reactive power sharing. In particular, the shaded bands represent the areas where the active power, reactive power and nodal voltages of all the CIG buses remain for every time instant. On the basis of the results, the following conclusions can be drawn. First, the active power control layer immediately adapts to the load changes, distributing the active power injections among the CIGs, and contributing to the frequency regulation. Thus, it can be seen that for both cases, i.e. with and without the OFO-based voltage control implementation, the active power injections are the same for all the CIGs. Second, the OFO-based secondary controller achieves a voltage profile always within the imposed technical limits, in contrast to the continuous under-voltage problems experienced in case of not implementing it. This is achieved with an excellent reactive power sharing, as shown in Fig. 11. Note that, however, the reactive power sharing deteriorates at some time instants because some operational constraints are transiently violated. For example, from $t = 19:00$ h to $t = 22:00$ h, some nodal voltages within the commercial feeder reach the upper voltage limit, 1.05 p.u. In that case, the secondary OFO-based controller guides the nodal voltages to the feasible area by reducing the corresponding CIG internal voltages. As a consequence, the MG reactive power sharing deteriorates as shown in Fig. 11 since the reactive power band widens during these hours.

Finally, Fig. 12 represents the evolution of the reactive power injections and the nodal voltages of the CIGs at buses R01, I02 and C16. These magnitudes are compared to the corresponding results of a model-based OPF with measurement updates every 10 min. As can be seen, the proposed control strategy adapts perfectly to the load changes, converging to the optimal solution computed by the OPF after a short transient period. Thus, it can be concluded that the proposed strategy adapts to changes of exogenous signals, e.g. load changes, converging to the optimal solution of the problem.

5. Conclusion

This paper has presented a real-time control methodology for AC MGs supplied by a set of controllable grid-forming CIGs. The methodology is based on a hierarchical two-layer control architecture. The primary control layer, implemented locally on each grid-forming CIG, emulates the performance of a synchronous generator that provides active power sharing, frequency and voltage support. The references of each individual grid-forming CIG is computed by the secondary control
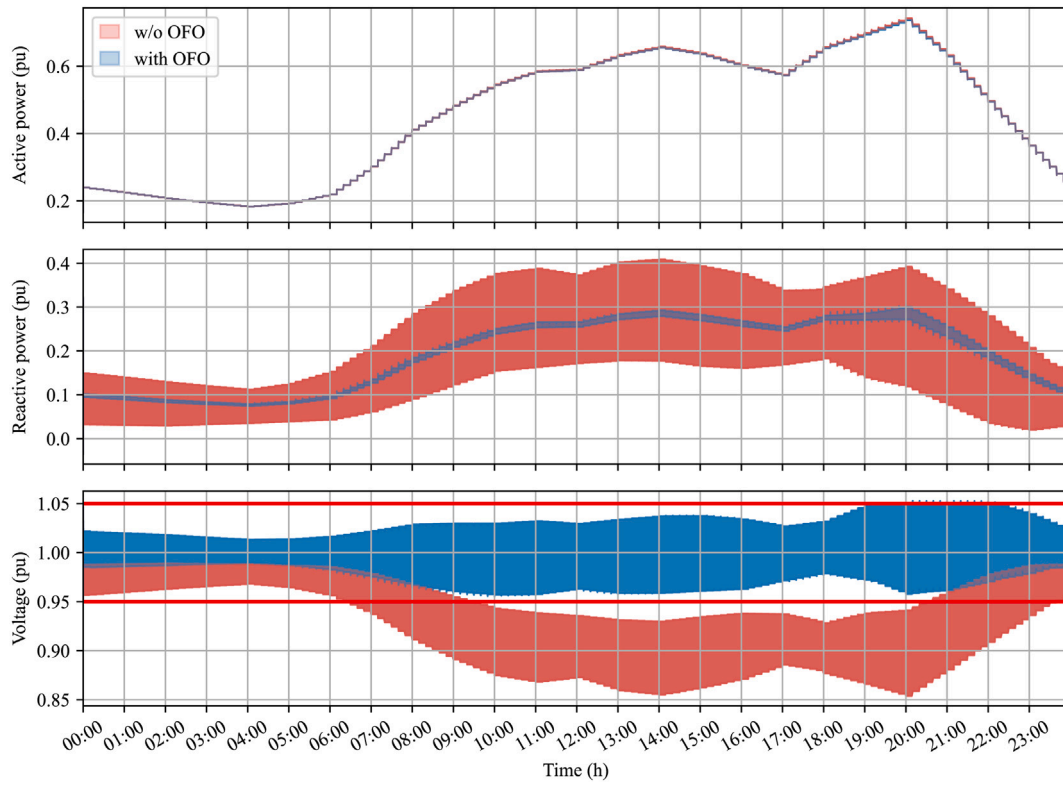
Fig. 11. MG based on the CIGRE European LV benchmark network. 24-hour simulation to evidence the impact of the proposed OFO-based controller on a large time period. $\alpha = 0.5 \cdot 10^{-4}$, $\beta_k = 500$, $\gamma_{k,j} = 10$, $\forall k, j \in \mathcal{V}_g$.
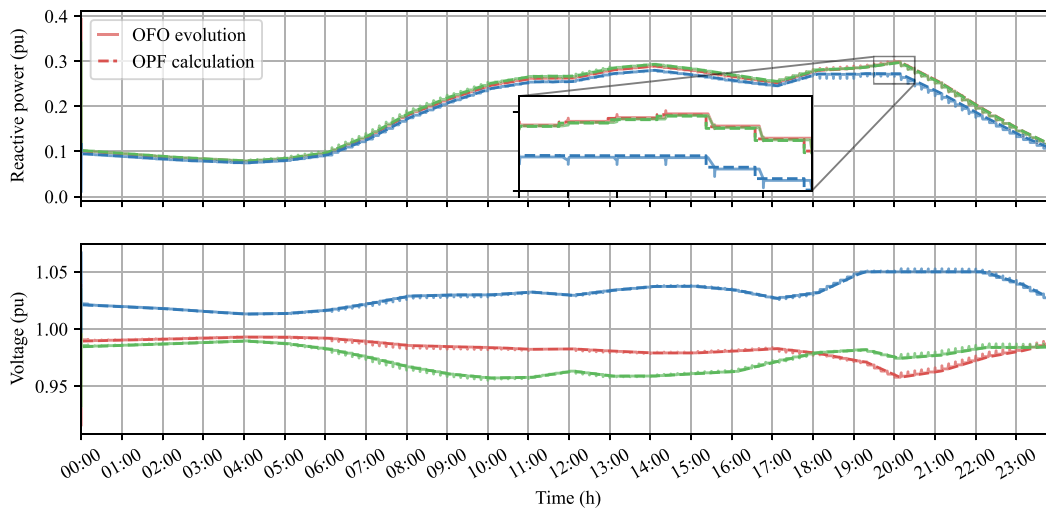

Fig. 12. MG based on the CIGRE European LV benchmark network. 24-hour simulation including a comparison with an OPF. CIGs connected to nodes R01 (red), I02 (green) and C16 (blue). Top plot: Reactive power injection. Bottom plot: Output voltage.

layer which is based on two independent applications. On the one hand, a conventional AGC is in charge of computing the active power setpoints to achieve grid frequency regulation. On the other hand, an OFO approach optimizes the nodal voltages and reactive power sharing between the controllable CIGs without resorting to a precise network model.

The paper has included some simulations on a small size MG for analyzing the method performance. The results evidence the good dynamic response of the algorithm, which is able to cope with large disturbances, restoring the nodal voltages within the limits and with reactive power sharing among the controllable CIGs. Even more, in order to strengthen the applicability of the proposed methodology a

HIL test of the secondary controller has been also discussed. In this regard, the real-time results perfectly resemble those obtained using an electromechanical simulation. Considering this, a long term simulation using a medium size MG has been carried out which has evidenced that the OFO-based controller solves voltage problems in an effective manner.

The main advantages of the proposed approach can be summarized as follows. First, it can be implemented in weak MGs leading to a good performance in terms of active and reactive power sharing between controllable assets and without resorting to a detailed network model. Second, the control architecture is resilient against communication failures since the local primary controllers maintain a stable MG operation.
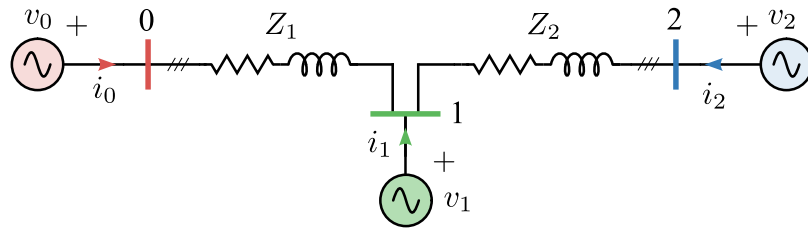
Fig. 13. Simple network used to derive the OFO matrix formulation.

Third, the proposed controller is robust enough since frequency and voltages of the MG are kept within the imposed operational limits even in case of some variables reach their technical bounds.

Future research lines will focus on the incorporation of additional network operational constraints, such as power line ampacity limits, within the OFO-based secondary control layer. Furthermore, the formulation of the proposed secondary controller in a distributed manner among grid-forming CIGs will be investigated.

Declaration of competing interest

The authors declare that they have no known competing financial interests or personal relationships that could have appeared to influence the work reported in this paper.

Data availability

All the data used in the paper are accessible (reference [38] of the manuscript)

Appendix. Example to illustrate the OFO matrix formulation

This appendix is devoted to illustrate how to derive the matrix formulation of the proposed OFO algorithm. For this purpose, consider the simple network depicted in Fig. 13, where three grid-forming CIGs, $N_g = 3$, connected through two branches, $N_b = 2$, are considered. Let $\mathcal{P} = \{(k, j) \; \forall k, j \in \mathcal{V}_g, k \neq j\}$ be the set of N_p possible pairs of CIGs within the network that, in the particular case depicted in Fig. 13, is defined as: $\mathcal{P} = \{(0, 1), (1, 2), (2, 0)\}$. The input and output vectors related to the proposed OFO-based voltage control are $\mathbf{u} = [V_{0,r}, V_{1,r}, V_{2,r}]^\top$ and $\mathbf{y} = [V_0, P_0, Q_0, V_1, P_1, Q_1, V_2, P_2, Q_2]^\top$ respectively. The reference output vector, $\mathbf{y}^\star$, is defined as a vector with the same dimension of the output vector, $\mathbf{y}$, which stacks the voltage references for each grid-forming CIG and zeros at the active and reactive power positions of $\mathbf{y}$ to make the cost functions in (3) and (5) equivalent. In particular, for the simple network shown in Fig. 13 $\mathbf{y}^\star = [V_0^\star, 0, 0, V_1^\star, 0, 0, V_2^\star, 0, 0]^\top$.

The matrix $\mathbf{Q}$ within (5) can be obtained in a systematic manner as follows:

$$\mathbf{Q} = \mathbf{M} \mathbf{A} \mathbf{R} \mathbf{A}^\top \mathbf{M}^\top + \mathbf{N} \boldsymbol{\beta} \mathbf{N}^\top \tag{8}$$

where:

- $\mathbf{A} \in \mathbb{R}^{N_g \times N_p}$ is the incidence matrix relating CIGs and CIGs pairs within the set $\mathcal{P}$.

- $\mathbf{R} \in \mathbb{R}^{N_p \times N_p}$ is a square diagonal matrix in which each diagonal term corresponds to each of the elements in $\mathcal{P}$. Thus, the matrix is constructed placing at each term the sum of the weighting parameters $\gamma_{k,j}$ and $\gamma_{j,k}$ for the pair $(k, j) \in \mathcal{P}$.

- $\mathbf{M} \in \mathbb{R}^{3N_g \times N_g}$ is a transformation matrix that selects the terms Q_k from the output vector $\mathbf{y}$. It is defined as $\mathbf{M} = \mathbf{I}_{N_g} \otimes [0, 0, 1]^\top$ where $\mathbf{I}_{N_g}$ denotes the identity matrix of dimension $N_g \times N_g$.

- $\mathbf{N} \in \mathbb{R}^{3N_g \times N_g}$ is a transformation matrix that selects the terms V_k from the output vector $\mathbf{y}$. It is defined as $\mathbf{N} = \mathbf{I}_{N_g} \otimes [1, 0, 0]^\top$.

- $\boldsymbol{\beta} \in \mathbb{R}^{N_g \times N_g}$ is a square diagonal matrix whose diagonal terms contain the weighting parameters β_k sorted in ascending order.

Particularizing these matrices for the network in Fig. 13 yields the following:

$$\mathbf{A} = \begin{bmatrix} 1 & 0 & -1 \\ -1 & 1 & 0 \\ 0 & -1 & 1 \end{bmatrix}, \; \mathbf{R} = \begin{bmatrix} \gamma_{0,1} + \gamma_{1,0} & 0 & 0 \\ 0 & \gamma_{1,2} + \gamma_{2,1} & 0 \\ 0 & 0 & \gamma_{0,2} + \gamma_{2,0} \end{bmatrix},$$

$$\boldsymbol{\beta} = \begin{bmatrix} \beta_0 & 0 & 0 \\ 0 & \beta_1 & 0 \\ 0 & 0 & \beta_2 \end{bmatrix}, \; \mathbf{M} = \mathbf{I}_3 \otimes \begin{bmatrix} 0 & 0 & 1 \end{bmatrix}^\top, \; \mathbf{N} = \mathbf{I}_3 \otimes \begin{bmatrix} 1 & 0 & 0 \end{bmatrix}^\top.$$

References

[1] (2021) I. World energy outlook 2021. Tech. rep., Paris: IEA; 2021.

[2] Lasseter RH. MicroGrids. In: 2002 IEEE power engineering society winter meeting. Conference proceedings (Cat. No.02CH37309), vol. 1. 2002, p. 305–8.

[3] Hatziargyriou N, Asano H, Iravani R, Marnay C. Microgrids. IEEE Power Energy Mag 2007;5(4):78–94.

[4] Rocabert J, Luna A, Blaabjerg F, Rodríguez P. Control of power converters in AC microgrids. IEEE Trans Power Electron 2012;27(11):4734–49.

[5] Olives-Camps JC, Mauricio JM, Barragán-Villarejo M, Matas-Díaz FJ. Voltage control of four-leg VSC for power system applications with nonlinear and unbalanced loads. IEEE Trans Energy Convers 2020;35(2):640–50.

[6] Lin Y, Eto JH, Johnson BB, Flicker JD, Lasseter RH, Villegas Pico HN, et al. Research roadmap on grid-forming inverters. Tech. rep., United States: National Renewable Energy Laboratory; 2020.

[7] De Brabandere K, Bolsens B, Van den Keybus J, Woyte A, Driesen J, Belmans R. A voltage and frequency droop control method for parallel inverters. IEEE Trans Power Electron 2007;22(4):1107–15.

[8] Wang X, Li YW, Blaabjerg F, Loh PC. Virtual-impedance-based control for voltage-source and current-source converters. IEEE Trans Power Electron 2015;30(12):7019–37.

[9] Guan M, Pan W, Zhang J, Hao Q, Cheng J, Zheng X. Synchronous generator emulation control strategy for Voltage Source Converter (VSC) stations. IEEE Trans Power Syst 2015;30(6):3093–101.

[10] Arghir C, Jouini T, Dörfler F. Grid-forming control for power converters based on matching of synchronous machines. Automatica 2018;95:273–82.

[11] Zhang W, Cantarellas AM, Rocabert J, Luna A, Rodriguez P. Synchronous power controller with flexible droop characteristics for renewable power generation systems. IEEE Trans Sustain Energy 2016;7(4):1572–82.

[12] Rosso R, Wang X, Liserre M, Lu X, Engelken S. Grid-forming converters: Control approaches, grid-synchronization, and future trends—A review. IEEE Open J Ind Appl 2021;2:93–109.

[13] Khayat Y, Shafiee Q, Heydari R, Naderi M, Dragičević T, Simpson-Porco JW, et al. On the secondary control architectures of AC microgrids: An overview. IEEE Trans Power Electron 2020;35(6):6482–500.

[14] Ma W, Wang W, Chen Z, Hu R. A centralized voltage regulation method for distribution networks containing high penetrations of photovoltaic power. Int J Electr Power Energy Syst 2021;129:106852.

[15] Xiao H, Liu G, Huang J, Hou S, Zhu L. Parameterized and centralized secondary voltage control for autonomous microgrids. Int J Electr Power Energy Syst 2022;135:107531.

[16] Khanalizadeh Eini M, Mirhosseini Moghaddam M, Tavakoli A, Alizadeh B. Improving the stability of hybrid microgrids by nonlinear centralized control in island performance. Int J Electr Power Energy Syst 2022;136:107688.

[17] Simpson-Porco JW, Shafiee Q, Dörfler F, Vasquez JC, Guerrero JM, Bullo F. Secondary frequency and voltage control of islanded microgrids via distributed averaging. IEEE Trans Ind Electron 2015;62(11):7025–38.

[18] Schiffer J, Seel T, Raisch J, Sezi T. Voltage stability and reactive power sharing in inverter-based microgrids with consensus-based distributed voltage control. IEEE Trans Control Syst Technol 2016;24(1):96–109.

[19] Zhang M, Li Y, Liu F, Lee W-J, Peng Y, Liu Y, et al. A robust distributed secondary voltage control method for islanded microgrids. Int J Electr Power Energy Syst 2020;121:105938.

[20] Dall'Anese E, Simonetto A. Optimal power flow pursuit. IEEE Trans Smart Grid 2018;9(2):942–52.

[21] Abdi H, Beigvand SD, Scala ML. A review of optimal power flow studies applied to smart grids and microgrids. Renew Sustain Energy Rev 2017;71:742–66.

[22] Bolognani S, Zampieri S. On the existence and linear approximation of the power flow solution in power distribution networks. IEEE Trans Power Syst 2016;31(1):163–72.

[23] Bai X, Wei H, Fujisawa K, Wang Y. Semidefinite programming for optimal power flow problems. Int J Electr Power Energy Syst 2008;30(6):383–92.

[24] Jabr R. Radial distribution load flow using conic programming. IEEE Trans Power Syst 2006;21(3):1458–9.

[25] Molzahn DK, Dörfler F, Sandberg H, Low SH, Chakrabarti S, Baldick R, et al. A survey of distributed optimization and control algorithms for electric power systems. IEEE Trans Smart Grid 2017;8(6):2941–62.

[26] Mansour M, Ellis J. Comparison of methods for estimating real process derivatives in on-line optimization. Appl Math Model 2003;27(4):275–91.

[27] Colombino M, Simpson-Porco JW, Bernstein A. Towards robustness guarantees for feedback-based optimization. In: 2019 IEEE 58th conference on decision and control. 2019, p. 6207–14.

[28] Colombino M, Dall'Anese E, Bernstein A. Online optimization as a feed-back controller: Stability and tracking. IEEE Trans Control Netw Syst 2020;7(1):422–32.

[29] Hauswirth A, Zanardi A, Bolognani S, Dörfler F, Hug G. Online optimization in closed loop on the power flow manifold. In: 2017 IEEE Manchester powertech. 2017, p. 1–6.

[30] Ortmann L, Hauswirth A, Caduff I, Dörfler F, Bolognani S. Experimental validation of feedback optimization in power distribution grids. Electr Power Syst Res 2020;189:106782.

[31] Picallo M, Bolognani S, Dörfler F. Closing the loop: Dynamic state estimation and feedback optimization of power grids. Electr Power Syst Res 2020;189:106753.

[32] Bolognani S, Carli R, Cavraro G, Zampieri S. On the need for communication for voltage regulation of power distribution grids. IEEE Trans Control Netw Syst 2019;6(3):1111–23.

[33] Ortmann L, Prostejovsky A, Heussen K, Bolognani S. Fully distributed peer-to-peer optimal voltage control with minimal model requirements. Electr Power Syst Res 2020;189:106717. http://dx.doi.org/10.1016/j.epsr.2020.106717.

[34] Häberle V, Hauswirth A, Ortmann L, Bolognani S, Dörfler F. Non-convex feedback optimization with input and output constraints. IEEE Control Syst Lett 2020;5(1):343–8.

[35] Kryonidis GC, Malamaki K-ND, Mauricio JM, Demoulias CS. A new perspective on the synchronverter model. Int J Electr Power Energy Syst 2022;140:108072.

[36] Luenberger DG, Ye Y. Linear and nonlinear programming. Springer Publishing Company, Incorporated; 2015.

[37] López-Erauskin R, González A, Petrone G, Spagnuolo G, Gyselinck J. Multi-variable perturb and observe algorithm for grid-tied PV systems with joint central and distributed MPPT configuration. IEEE Trans Sustain Energy 2021;12(1):360–7.

[38] Olives-Camps JC, Rodríguez del Nozal A, Mauricio JM, Maza-Ortega JM. A model-less control algorithm of DC microgrids based on feedback optimization. Int J Electr Power Energy Syst 2022;141:108087.

[39] Strunz K, et al. Benchmark systems for network integration of renewable and distributed energy resources. 2014, p. 119, CIGRE Task Force C6.04.02.